Modeling and Pointing Performance Analysis of Disturbance-Free-Payload System With Flexible Umbilical Connection

JIAXING ZHOU[1,2], **ZHIGANG WANG**[1,2], **WEI LI**[1,2], **LEI LIU**[1,2], **YIFAN DENG**[3], **AND QIANG ZHAO**[4]

[1]School of Astronautics, Northwestern Polytechnical University, Xi'an 710072, China
[2]National Key Laboratory of Aerospace Flight Dynamics, Northwestern Polytechnical University, Xi'an 710072, China
[3]School of Electronic and Information Engineering, Xi'an Jiaotong University, Xi'an 710049, China
[4]Shanghai Satellite Engineering Institute, Shanghai 201109, China

Corresponding author: Zhigang Wang (sbeotal@nwpu.edu.cn)

ABSTRACT Disturbance-Free-Payload is a novel spacecraft architecture proposed to achieve perfect vibration isolation performance of space applications. In this paper, the object under study is a DFP system in which a flexible umbilical connection between the support module (SM) and the payload module (PM) is introduced for data, power and fluid transfer. Bead model accounting for properties of mass and flexibility, is utilized to model the flexible umbilical. With incorporation of bead model, six degree-of-freedom multibody rigid-flexible dynamics for the DFP system is established via Newtonian mechanics. Along with rotational coupling between solar panels and SM, translational coupling, in particular, is taken into consideration since there is a stringent requirement on relative position between PM and SM. Based on the accurate motion equations of the DFP system, simulation studies are conducted to gain insight of the impact of umbilical connection and translational coupling on pointing performance of the DFP system. Simulation results validate effectiveness of DFP configuration in isolating vibrations transmitted from SM to PM. Besides, umbilical connection plays an important part in degrading pointing performance of PM whereas it exerts little impact on SM. Moreover, translational coupling leads to significant pointing performance degradation for both PM and SM.

INDEX TERMS Disturbance-Free-Payload, vibration control, pointing performance, bead model.

I. INTRODUCTION

Space-borne missions relating to earth observation, astrometry and meteorology, raise stringent requirements for vibration mitigation and pointing performance [1]–[4]. For instance, the solar observations satellite (SOLAR-B) imposes requirement on short-term pointing stability of 0.06 arcsec and the Nearby Earth Astrometric Telescope (NEAT) is designed to achieve sub-micro-arcsecond (0.05 μ as) pointing stability for extremely-high-precision astrometric measurements [3], [5]. Moreover, astrophysical missions associated with dark energy and dark matter, in particular, make highly precise pointing resolution requirement on spacecraft system to detect photometric redshifts [6].

To meet the demands proposed by these missions, vibration isolation techniques are urgently needed. Traditional vibration isolation methods include passive and active isolation [7], [8]. Passive isolators are capable of providing vibration suppression performance and stability in the high frequency range (100 Hz and above) without external power input. However, vibration isolation performance of passive isolators is limited within low frequency region (0 to 100 Hz) [9]. In order to address the challenge of low frequency vibration isolation, various studies are dedicated to active isolation techniques [9], [10]. Active isolators have proved to achieve excellent vibration isolation, especially in the low frequency range at the expense of external energy

The associate editor coordinating the review of this manuscript and approving it for publication was Ning Sun.

cost and weight increase of spacecraft system. Therefore, a trade-off between vibration isolation performance and the resulting extra cost should be carefully considered to achieve optimum mission performance within a constrained budget. As vibration isolation and pointing performance demands increase, traditional isolation techniques are hardly capable of meeting extremely high performance imposed by modern and even future space-borne missions.

To tackle this problem, a new configuration named Disturbance-Free-Payload (DFP), which is thought to be able to effectively isolate micro-vibration transmitted from spacecraft to sensitive payload, was proposed by Pedreiro [11]. A basic architecture of the DFP consists of two modules, a support module (SM) and a payload module (PM). The payload module, which is separated from the support module and is working as an individual module, requires precision control and high stability, whereas the support module does not. Despite environmental disturbances, the support module, which carries mission support equipments, contains the main onboard vibration sources, such as reaction wheels and flexible solar panels. The noncontact interface consisting of noncontact sensors and noncontact actuators between the two modules, is used for relative motion control and thus contributes to attenuate the onboard vibrations transmitted from the support module to the payload module [12].

However, the DFP configuration is still under testing stage rather than being mature for real space missions since mechanical connection like umbilical is still needed for power, data and fluid transfers. Thus, the impact of the mechanical connection on the pointing performance of the DFP system should be investigated thoroughly. Among the studies that deal with this problem, research study in Ref [13], which aims at analyzing dynamics of the DFP system, appears to be the first effort that established the mathematic model for electrical cables connection between the support and payload modules. In this model, the stiffness of the cable was considered. Ref [14] simply used cable model and stiffness matrix in Ref [13] to extensively study the coupling characteristics between the PM and SM. In spite of stiffness of umbilical, some researchers take the flexibility property into account. Ref [15] first study dynamics modeling of a separated satellite with flexible cable. The cable in this work was modeled as a translational spring/damper element. Simulation results indicate that the flexible greatly reduced the pointing performance of the DFP system. Furthermore, Ref [16] extends the work in Ref [15] by considering both of translational effects and torsional effects of the flexible cable. Simulation results show that the umbilical significantly lowers natural frequency of the payload and greatly degrades the pointing performance. Comparison between cases considering and not considering torsional effects of the umbilical shows that torsional stiffness exerts weak influence on the pointing performance.

It should be noted that, the flexible cable/umbilical models in the mentioned works do not exactly consider flexibility property since a single spring/damper element could not precisely depict flexible characteristics of cables/umbilicals. Besides, the mass of the cable/umbilical is ignored which might make the model less reliable. Furthermore, these models are unable to depict the shape of cables/umbilcials which is important to study interaction between cables/umbilicals and the support module (or payload module).

Though the aforementioned works provide certain foundation for investigation of DFP system with umbilical connection, precise umbilical model covering properties of flexibility and mass remains unexplored.

Solar panels have been employed to supply sustained electrical power for most spacecraft systems. During the process of space mission implementation, disturbances onboard the spacecraft might trigger elastic vibrations of the solar panels which will degrade performance of payloads in spacecraft [17]. To deal with the resulting flexible-rigid coupling dynamics problem, most literature consider the rotational coupling between the spacecraft and flexible appendages whereas the translational coupling is excluded for the fact that it makes little impact on attitude motion of the spacecraft system. Since a critical distance between the PM and SM must be guaranteed to prevent the noncontact sensors and actuators from going out of range (± 5 mm) [18], the translational coupling between the SM and solar panels, however, should not be ignored for the DFP system.

This paper is dedicated to revealing the impact of umbilical and solar panels on pointing performance of the DFP system and its main contribution lies in: 1) bead model [19] which can account for mass and flexibility properties of umbilical is incorporated in the dynamics of the DFP system and its impact on pointing performance of DFP system is analyzed through simulation studies, 2) along with rotational coupling between the support module and the solar panels, the translational coupling is taken into consideration in order to obtain reliable simulation results, and the impact of translational coupling on pointing performance of DFP system is investigated.

The remainder of this paper is organized as follows: Section II gives a detailed description of the DFP system with umbilical connection. Description involving basic configuration and vectors description of DFP system is presented. Section III is devoted to the establishment of multibody rigid-flexible dynamics of the DFP system. Then, simulation studies are performed in Section IV. Finally, Section V concludes the paper.

II. DFP SYSTEM DESCRIPTION
A. BASIC CONFIGURATION OF DFP SYSTEM UNDER STUDY
A basic configuration of DFP system under study in this paper is presented in Fig. 1. As can be seen, the concerned DFP system consists of two modules, a payload module and a support module connecting with two flexible solar panels. The key design that effectively isolate vibrations transmitted from SM to PM is the DFP interface between SM and PM, which
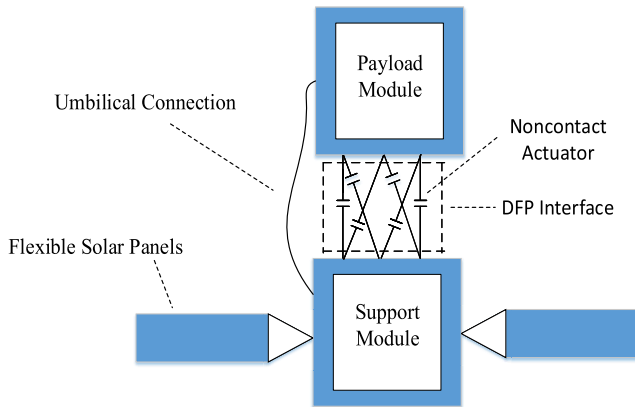
FIGURE 1. Basic configuration of DFP system with umbilical connection.
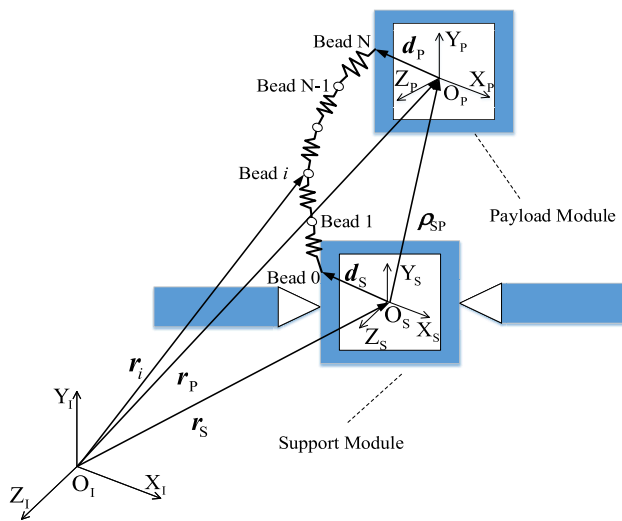

FIGURE 2. Vector description of the DFP system.

consists of 6 position sensors and 6 noncontact actuators. The actuators and sensors are installed in a hexapod configuration. A possible noncontact actuator design could be noncontact voice coil actuator [20].

The only difference between the concerned DFP configuration and the ideal configuration lies in that the former one uses an umbilical connection between the PM and SM for energy, data and fluid transfer, whereas the latter one does not.

B. VECTORS DESCRIPTION OF DFP SYSTEM

In order to further our understanding about the umbilical connection between the SM and PM, bead model which simultaneously covers properties of flexibility and mass of the umbilical is incorporated in the DFP system.

Figure 2 illustrates a detailed vector description of the DFP system under study, as well as reference coordinate frames employed in this paper. As can be seen, the umbilical is discretized into N-1 point-mass beads (numbered from 1 to N-1) each interconnected by one spring. Thus, this system is

composed of two modules (namely, SM and PM) and N-1 point masses. It should be noted that bead 0 represent the junction point of the umbilical and SM. Likewise, bead N denotes the junction point of the umbilical and PM. Instead of taking bending and torsional stiffness into account, only axial stiffness is considered in bead model since extension behavior of the umbilical is the main concern in this paper. Besides, the inclusion of bending and torsional behaviors involves a substantial increase in the complexity of the analysis.

The *J2000 Equatorial Reference Frame* O_I-$X_IY_IZ_I$ is utilized for mathematical description of the DFP system. O_I is the origin of the reference frame which lies at the Earth's center of mass. X-axis points toward the vernal equinox, while Y-axis is 90° to the east in the equatorial plane. Z-axis directs along the north pole. The body-fixed frame O_S-$X_SY_SZ_S$ is a principal axis frame of the SM with axes along the principal central axes of inertial. Similarly, the other body-fixed frame O_P-$X_PY_PZ_P$ is a principal axis frame of the PM.

r_S, r_P and r_i ($i = 1 \sim N-1$) are position vectors of the center of mass of the SM, PM and bead i, respectively. Besides, r_1 and r_N are position vectors of junction point. All vectors defined above are measured relative to the origin of inertial frame O_I-$X_IY_IZ_I$. $\rho_{SP} = r_P - r_S$ is a vector used to show the relative position vector between SM and PM. d_S is the position vector of junction point associated with SM measured along O_S-$X_SY_SZ_S$ while d_P is its counterpart resolved in O_P-$X_PY_PZ_P$. In addition, $\rho_i = r_i - r_{i-1}$ stands for relative position between bead i and bead i-1.

III. MULTIBODY RIGID-FLEXIBLE DYNAMICS OF DFP SYSTEM

As mentioned in last section, this system is composed of N+1 bodies, namely two modules (SM and PM) and N-1 point masses. Motion equations for SM, PM and N-1 beads are derived via Newtonian mechanics. In order to facilitate the modeling procedure and analysis in later part, the following assumptions are made:

1) Both of length and stiffness of all elastic strings in the bead model are assumed to be identical.

2) The noncontact interface which consists of six noncontact actuators in a hexapod configuration, is regarded as a generalized actuator. The generalized actuator generates resultant control force and resultant control torque.

3) The sensors error is neglected.

Since the main emphasis of this paper is on studying the influence of umbilical connection on DFP system, practical issues like input saturation, input dead zones and parametric uncertainties and unmodeled dynamics are neglected. However, in real-world applications, practical systems including DFP system are inevitably suffering these engineering issues.

These engineering issues are widely investigated and possible approaches are proposed. To address control problem of double-pendulum cranes, Ref [21] proposes a new quasi-proportional integral derivative control method which incorporates both integral action and actuating constraints without any linearizing operations and can works well in

the presence of unmodeled dynamics. In addition, to tackle control problems like input dead zones of underactuated ship-mounted crane systems, Ref [22] presents a neural network-based adaptive anti-swing control approach which proves to be effective in dealing with unknown/uncertainty parameters/structures in ship-mounted crane dynamics and nonlinear input dead zones in servo motors. The effectiveness and practicality of the mentioned control approaches in Ref [11], [21], [22] are verified by experiment and their robustness are guaranteed. Thus, these control approaches are promising solutions to address engineering issues confronting the DFP system in this paper.

Motion equations for the DFP system are derived after an analysis of forces and moments acting on the system.

A. ANALYSIS OF FORCES AND MOMENTS ACTING ON THE DFP SYSTEM

The PM motion is subject to the following forces and moments: 1) the Earth gravity $\boldsymbol{F}_{\mathrm{Pg}}$, 2) disturbing force and moment $\boldsymbol{F}_{\mathrm{Pd}}$ and T_{Pd}, 3) umbilical force $\boldsymbol{F}_{\mathrm{Pu}}$ and moment $\boldsymbol{T}_{\mathrm{Pu}}$ acting on the PM, 4) control force $\boldsymbol{F}_{\mathrm{Pc}}$ and torque $\boldsymbol{T}_{\mathrm{Pc}}$ applied by the generalized noncontact actuator.

The SM motion is susceptible to the following forces and moments: 1) the Earth gravity $\boldsymbol{F}_{\mathrm{Sg}}$, 2) disturbing force and moment $\boldsymbol{F}_{\mathrm{Sd}}$ and $\boldsymbol{T}_{\mathrm{Sd}}$, 3) umbilical force $\boldsymbol{F}_{\mathrm{Su}}$ and moment $\boldsymbol{T}_{\mathrm{Su}}$ acting on the SM, 4) control torque $\boldsymbol{T}_{\mathrm{Sc}}$ applied by external actuators like reaction wheels and thrusters, 5) interaction force and moment applied by noncontact actuator, $\boldsymbol{F}_{\mathrm{Sint}}$ and $\boldsymbol{T}_{\mathrm{Sint}}$.

Since the beads in the bead model are point masses, the forces acting on each of them simply include two spring forces and Earth gravity ($\boldsymbol{F}_{ig}$). The resultant spring force acting on bead i is denoted as $\boldsymbol{F}_{\mathrm{B}i}$.

A detailed introduction of all the forces and moments is given below.

1) EARTH GRAVITY F_{Pg}, F_{Sg} AND F_{ig}

The PM gravity force $\boldsymbol{F}_{\mathrm{Pg}}$ is defined by:

$$\boldsymbol{F}_{\mathrm{Pg}} = M_{\mathrm{P}} \cdot \nabla U_{\mathrm{P}} \tag{1}$$

where U_{P} is the Earth gravitational potential which can be given by a summation of all possible spherical harmonics [23].

By substituting subscript 'P' to 'S' in (1), $\boldsymbol{F}_{\mathrm{Sg}}$ can be obtained:

$$\boldsymbol{F}_{\mathrm{Sg}} = M_{\mathrm{S}} \cdot \nabla U_{\mathrm{S}} \tag{2}$$

where U_{S} is counterpart of U_{P}.

Similarly, Earth gravity acting on bead i can be calculated as:

$$\boldsymbol{F}_{ig} = M_i \cdot \nabla U_i \tag{3}$$

2) DISTURBING FORCES AND MOMENTS F_{PD}, F_{Sd}, T_{Pd} AND T_{Sd}

Here, we assume the DFP system under study operate at low Earth orbit. Thus, atmospheric drag plays the major part

whereas other disturbing forces like radiation force can be neglected.

$\boldsymbol{F}_{\mathrm{Pd}}$ and $\boldsymbol{F}_{\mathrm{Sd}}$ are expressed as:

$$\boldsymbol{F}_{\mathrm{Sd}} = -\frac{1}{2} C_{\mathrm{d}} S_{\mathrm{d}} \rho \left\| \boldsymbol{v}_{\mathrm{Sr}} \right\| \boldsymbol{v}_{\mathrm{Sr}}$$

$$\boldsymbol{F}_{\mathrm{Pd}} = -\frac{1}{2} C_{\mathrm{d}} S_{\mathrm{d}} \rho \left\| \boldsymbol{v}_{\mathrm{Pr}} \right\| \boldsymbol{v}_{\mathrm{Pr}} \tag{4}$$

where C_{d} is the drag coefficient, S_{d} is the reference area, ρ is the atmospheric density, $\boldsymbol{v}_{\mathrm{Sr}}$ is the satellite velocity relative to the rotating atmosphere, $\left\| \boldsymbol{v}_{\mathrm{Sr}} \right\|$ is the norm of $\boldsymbol{v}_{\mathrm{Sr}}$. $\left\| \boldsymbol{v}_{\mathrm{Pr}} \right\|$ and $\boldsymbol{v}_{\mathrm{Pr}}$ are counterparts of $\left\| \boldsymbol{v}_{\mathrm{Sr}} \right\|$ and $\boldsymbol{v}_{\mathrm{Sr}}$, respectively [24].

Disturbing moments acting on the SM consist of gravity gradient moment and disturbing moments resulted from devices inside the SM like wheel actuators. Gravity gradient moment expressed in the body-fixed frame O_{S}-$X_{\mathrm{S}}Y_{\mathrm{S}}Z_{\mathrm{S}}$ is presented:

$$T_{\mathrm{SDg}}^{\mathrm{b}} = \frac{3\mu}{\left| r_{\mathrm{S}}^{\mathrm{b}} \right|^5} \begin{bmatrix} \left(I_{\mathrm{S}z} - I_{\mathrm{S}y} \right) r_{\mathrm{S}y}^{\mathrm{b}} r_{\mathrm{S}z}^{\mathrm{b}} \\ \left(I_{\mathrm{S}x} - I_{\mathrm{S}z} \right) r_{\mathrm{S}x}^{\mathrm{b}} r_{\mathrm{S}z}^{\mathrm{b}} \\ \left(I_{\mathrm{S}y} - I_{\mathrm{S}x} \right) r_{\mathrm{S}x}^{\mathrm{b}} r_{\mathrm{S}y}^{\mathrm{b}} \end{bmatrix} \tag{5}$$

where $\mu = 3.9860044 \times 10^{14} \mathrm{m}^3/\mathrm{s}^2$ is the standard gravitational parameter, $r_{\mathrm{S}}^{\mathrm{b}} \left(r_{\mathrm{S}x}^{\mathrm{b}}, r_{\mathrm{S}y}^{\mathrm{b}}, r_{\mathrm{S}z}^{\mathrm{b}} \right)$ represents three components of r_{S} resolved along O_{S}-$X_{\mathrm{S}}Y_{\mathrm{S}}Z_{\mathrm{S}}$.

Disturbance produced by the movement of equipments and instruments are the main source of disturbing moments onboard the SM. For simplicity, the disturbing moments onboard the SM in this paper is regarded as a combination of constant and sinusoidal disturbing moments:

$$T_{\mathrm{SDw}}^{\mathrm{b}} = \begin{bmatrix} 2 \times 10^{-3} \\ -3 \times 10^{-3} \\ 4 \times 10^{-3} \end{bmatrix} \mathrm{N} \cdot \mathrm{m}$$

$$+ \begin{bmatrix} 1 \times 10^{-3} \cos \left(0.0106t \right) \\ -4 \times 10^{-3} \sin \left(0.0106t \right) \\ 4 \times 10^{-3} \sin \left(0.0106t \right) \end{bmatrix} \mathrm{N} \cdot \mathrm{m} \tag{6}$$

Then, the disturbing moments acting on the SM can be calculated with following expression:

$$T_{\mathrm{Sd}} = T_{\mathrm{SDg}}^{\mathrm{b}} + T_{\mathrm{SDw}}^{\mathrm{b}} \tag{7}$$

Thanks to the noncontact configuration, the PM is immune from disturbance onboard the SM. Therefore, gravity gradient moment is the only source of disturbance. With a similar form of (5), the disturbing moments applying on the PM is presented as:

$$T_{\mathrm{Pd}} = T_{\mathrm{PDg}}^{\mathrm{b}} = \frac{3\mu}{\left| r_{\mathrm{P}}^{\mathrm{b}} \right|^5} \begin{bmatrix} \left(I_{\mathrm{P}z} - I_{\mathrm{P}y} \right) r_{\mathrm{P}y}^{\mathrm{b}} r_{\mathrm{P}z}^{\mathrm{b}} \\ \left(I_{\mathrm{P}x} - I_{\mathrm{P}z} \right) r_{\mathrm{P}x}^{\mathrm{b}} r_{\mathrm{P}z}^{\mathrm{b}} \\ \left(I_{\mathrm{P}y} - I_{\mathrm{P}x} \right) r_{\mathrm{P}x}^{\mathrm{b}} r_{\mathrm{P}y}^{\mathrm{b}} \end{bmatrix} \tag{8}$$

3) UMBILICAL FORCES AND MOMENTS, F_{Su}, F_{Pu}, $\mathbf{F}_{\mathrm{B}i}$, T_{Pu} AND T_{Su}

The umbilical force and moment acting on the SM can be expressed as:

$$\boldsymbol{F}_{\mathrm{Su}} = k_{\mathrm{s}} \left(\boldsymbol{\rho}_1 - \bar{l}_{\mathrm{s}} \frac{\boldsymbol{\rho}_1}{\left\| \boldsymbol{\rho}_1 \right\|} \right) \tag{9}$$

$$T_{Su} = d_S \times F_{Su} \qquad (10)$$

where $\|\boldsymbol{\rho}_1\|$ is norm of ρ_1 and k_s is stiffness of elastic spring. l_s is length of elastic spring when the spring reaches a state of equilibrium, i.e., a state that spring has no deformation. The relationship between parameters of elastic spring (k_s, l_s and M_i) and their counterparts of umbilical (stiffness k_u, length l_u and M_u) are given as:

$$
\begin{aligned}
k_s &= N k_u \\
\bar{l}_s &= \frac{\bar{l}_u}{N} \\
M_i &= \frac{M_u}{N-1}
\end{aligned} \qquad (11)
$$

Similarly, the umbilical force and moment applying on the PM are:

$$F_{Pu} = -k_s \left(\boldsymbol{\rho}_N - \bar{l}_s \frac{\boldsymbol{\rho}_N}{\|\boldsymbol{\rho}_N\|} \right) \qquad (12)$$

$$T_{Pu} = d_P \times F_{Pu} \qquad (13)$$

As for bead i, the spring forces acting by adjacent beads (i.e. bead i-1 and bead i+1) are presented below:

$$
\begin{aligned}
F_{Bi1} &= -k_s \left(\boldsymbol{\rho}_i - \bar{l}_s \frac{\boldsymbol{\rho}_i}{\|\boldsymbol{\rho}_i\|} \right) \\
F_{Bi2} &= k_s \left(\boldsymbol{\rho}_{i+1} - \bar{l}_s \frac{\boldsymbol{\rho}_{i+1}}{\|\boldsymbol{\rho}_{i+1}\|} \right)
\end{aligned} \qquad (14)
$$

Thus, the resultant force (F_{Bi}) acting on bead i can be obtained:

$$
\begin{aligned}
F_{Bi} &= F_{Bi1} + F_{Bi2} \\
&= k_s \left(\boldsymbol{\rho}_{i+1} - \bar{l}_s \frac{\boldsymbol{\rho}_{i+1}}{\|\boldsymbol{\rho}_{i+1}\|} \right) - k_s \left(\boldsymbol{\rho}_i - \bar{l}_s \frac{\boldsymbol{\rho}_i}{\|\boldsymbol{\rho}_i\|} \right)
\end{aligned} \qquad (15)
$$

4) CONTROL FORCES AND TORQUES OF DFP SYSTEM, F_{Pc}, T_{Pc} and T_{Sc}

As is shown in Fig. 3, DFP control system includes three control loops, PM attitude control loop (controlled by T_{Pc}), relative position control loop (controlled by F_{Pc}) and relative attitude control loop (controlled by T_{Sc}) between PM and SM. The three control laws are given in Section III-B.

5) INTERACTION FORCE AND MOMENT APPLIED BY NONCONTACT ACTUATOR, F_{Sint} and T_{Sint}

It should be noted that F_{Sint} and F_{Pc} are an interaction pair. Thus, F_{Sint} can be expressed as:

$$F_{Sint} = -F_{Pc} \qquad (16)$$

Then, the resulting moment T_{Sint} is calculated by the following formula:

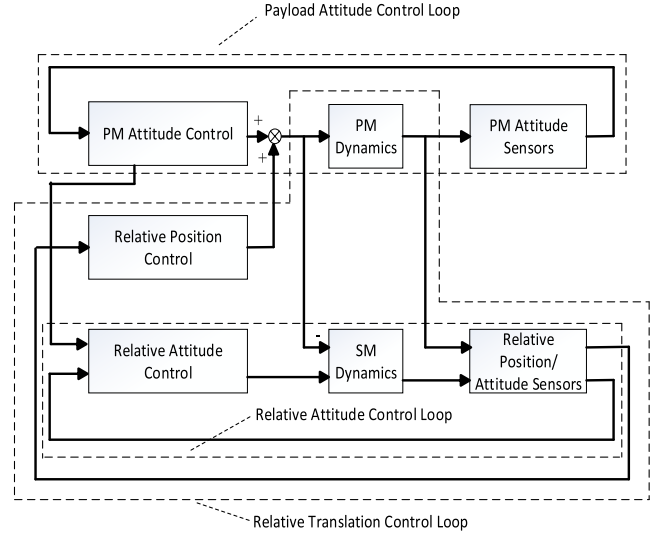$$T_{Sint} = -T_{Pc} + \boldsymbol{\rho}_{SP} \times F_{Sint} \qquad (17)$$

FIGURE 3. DFP control architecture.

B. 6-DOF MOTION EQUATIONS OF PM AND SM

The motion equations consist of kinematic and dynamic equations of the payload module. The kinematic equations can be expressed as:

$$
\begin{aligned}
\dot{r}_P &= v_P \\
\dot{q}_P &= \frac{1}{2} q_P \otimes \boldsymbol{\varpi}_P
\end{aligned} \qquad (18)
$$

The dynamic equations are given as follows.

$$
\begin{aligned}
M_P \dot{v}_P &= M_P a_P = F_{Pg} + F_{Pd} + F_{Pu} + F_{Pc} \\
I_P \dot{\omega}_P &= -\omega_P \times (I_P \omega_P) + T_{Pd} + T_{Pu} + T_{Pc}
\end{aligned} \qquad (19)
$$

where M_P and I_P are the mass and inertial tensor of the PM, respectively. v_P and a_P are translational velocity and translational acceleration, respectively. ω_P and $\boldsymbol{\varpi}_P = \left(0 \ \omega_P^T \right)^T$ are angular velocity and its expanded form. The superscript T denotes transpose operator. $q_P = \left(q_{P0} \ q_{Pv}^T \right)^T$ is quaternion of PM relative to inertial frame in which q_{P0} is scalar part and q_{Pv} is vector part. Rotation sequence 'Z-Y-X' is used in this paper with three corresponding Euler angles ψ_P, θ_P and φ_P.

Motion equations consisting of kinematic and dynamic equations of the SM installed with flexible solar panel are derived by using hybrid coordinate method and are presented below:

$$
\begin{aligned}
\dot{r}_S &= v_S \\
\dot{q}_S &= \frac{1}{2} q_S \otimes \boldsymbol{\varpi}_S
\end{aligned} \qquad (20)
$$

$$
\begin{aligned}
M_S \dot{v}_S + B_t \ddot{\eta} &= F_{Sg} + F_{Sd} + F_{Su} \\
I_S \dot{\omega}_S + B_r \ddot{\eta} &= -\omega_S \times (I_S \omega_S) + T_{Sd} + T_{Su} + T_{Sc} \\
\ddot{\eta} + 2\zeta\Omega\dot{\eta} + \Omega^2\eta + B_t^T a_S + B_r^T \dot{\omega}_S &= 0
\end{aligned} \qquad (21)
$$

in which the quantities with subscript S are counterparts of quantities associated with PM in (18) and (19). In addition, η represents modal coordinates. ζ and Ω denote the modal

damping ratio and fundamental frequencies of the solar panels, respectively. B_t and B_r are translational matrix and rotational coupling matrix which represent the coupling effect between the solar panels and the SM.

To address the composite control problem, three proportional-derivative controllers are designed:

$$
\begin{aligned}
\boldsymbol{T}_{Pc} &= K_{PP} \left(q_{Pv0} - q_{Pv} \right) + K_{PD} \left(\boldsymbol{\omega}_{P0} - \boldsymbol{\omega}_P \right) \\
\boldsymbol{F}_{Pc} &= K_{RTP} \left(\boldsymbol{\rho}_{SP0} - \boldsymbol{\rho}_{SP} \right) + K_{RTD} \left(\dot{\boldsymbol{\rho}}_{SP0} - \dot{\boldsymbol{\rho}}_{SP} \right) \\
\boldsymbol{T}_{Sc} &= K_{RAP} \left(q_{Rv0} - q_{Rv} \right) + K_{RAD} \left(\boldsymbol{\omega}_{R0} - \boldsymbol{\omega}_R \right)
\end{aligned} \quad (22)
$$

where K_{PP}, K_{RTP} and K_{RAP} are proportional gains. K_{PD}, K_{RTD} and K_{RAD} are derivative gains. q_{Pv0} is vector part of desired PM quaternion while $\boldsymbol{\omega}_{P0}$ is desired angular velocity of PM. $\boldsymbol{\rho}_{SP0}$ and $\dot{\boldsymbol{\rho}}_{SP0}$ are desired relative positive vector and desired relative velocity vector. q_{Rv} and q_{Rv0} are real-time and desired vector part of a new quaternion and desired vector part of a new quaternion $q_R = \left(q_{R0} \ q_{Rv}^T \right)^T$ which represents rotation between body-fixed frame O_S-$X_S Y_S Z_S$ and O_P-$X_P Y_P Z_P$. Likewise, $\boldsymbol{\omega}_R$ and $\boldsymbol{\omega}_{R0}$ are real-time and desired relative angular velocity.

C. MOTION EQUATION OF BEADS
As is shown in Fig. 2, motion of bead i are affected by Earth gravity and two adjacent spring forces. Therefore, the kinematic and dynamic equation of bead i can be given as:

$$
\boldsymbol{v}_i = \dot{\boldsymbol{r}}_i \quad (23)
$$

$$
M_i \dot{\boldsymbol{v}}_i = \boldsymbol{F}_{ig} + k_s \left(\boldsymbol{\rho}_{i+1} - l_s \frac{\boldsymbol{\rho}_{i+1}}{\|\boldsymbol{\rho}_{i+1}\|} \right) - k_s \left(\boldsymbol{\rho}_i - l_s \frac{\boldsymbol{\rho}_i}{\|\boldsymbol{\rho}_i\|} \right) \quad (24)
$$

Due to the point-mass assumption of the bead model, rotational motion is not considered.

IV. VERIFICATION OF BEAD MODEL
The Bead Model is previously used in tethered satellite and is thought to be capable of considering umbilical properties of flexibility and mass. However, whether this model could be used to model the mechanical connection between PM and SM in the DFP system remains a problem. With the help from Shanghai Satellite Engineering Institute, a thorough set of experiments on umbilical connection have been conducted and the relevant results are also provided. Experimental apparatus, which consists of a payload module and a support module with umbilical connection between them is shown in Fig. 4. By reducing the distance between the two modules, the umbilical force changes accordingly. An electronic scale between umbilical and the support module is used to measure the umbilical force.

Simulation concerning bead model (Fig. 5) applied in this paper and single spring model (Fig. 6) used in previous literature are performed.

Variation of umbilical force versus variation of relative position vector $-\Delta \rho_{SP}$ in experiments and simulations associated with bead model and single spring model are presented in Fig. 7. As can be seen in Fig. 7, the fact that there is a
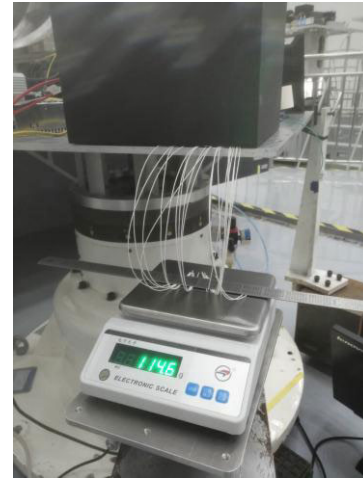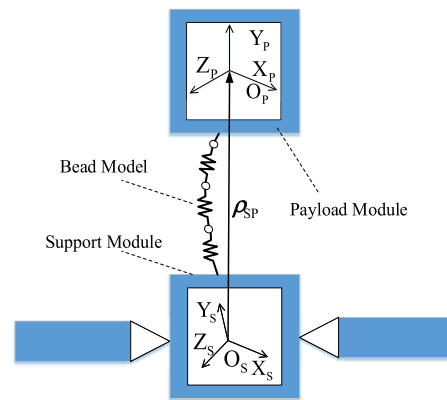

FIGURE 4. DFP experimental apparatus.

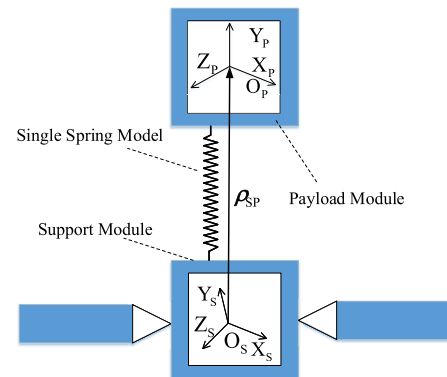**FIGURE 5.** DFP system with bead model.

FIGURE 6. DFP system with single spring model.

considerable difference between the results of single spring model and experiments while comparably little difference is witnessed between the results of bead model and experiments, verifies the accuracy of bead model.

V. SIMULATION STUDIES
In this section, we apply the DFP system in inertial orientation mission. Simulation studies on pointing performance of DFP

TABLE 1. Simulation conditions.

| Variable	Variable Name	Value
$M_S(\text{kg})$	Mass of SM	2334.3
$I_S(\text{kg}\cdot\text{m}^2)$	Moment of Inertial of SM	$\text{diag}(4552.64 \quad 4884.994 \quad 6992.726)$
$M_P(\text{kg})$	Mass of PM	100
$I_P(\text{kg}\cdot\text{m}^2)$	Moment of Inertial of PM	$\text{diag}(86.215 \quad 85.07 \quad 113.565)$
$a(\text{km})$	Semimajor Axis of Nominal Orbit	6598.145
e	Eccentricity of Nominal Orbit	0
$I(°)$	Inclination of Nominal Orbit	0
$\Omega_{\text{orbit}}(°)$	Longitude of the Ascending Node	0
$\omega(°)$	Argument of Periapsis	0
$\psi(°)$	True Anomaly at Epoch	0
$l_u(\text{m})$	Length of Umbilical	1
$k_u(\text{N}/\text{m})$	Stiffness of Umbilical	40
$M_u(\text{kg})$	Mass of Umbilical	1
N	Bead Number	20
$d_S(\text{m})$	Position of Junction Point Associated with PM	$(-0.3 \quad -0.4 \quad -0.5)$
$d_S(\text{m})$	Position of Junction Point Associated with SM	$(-0.1 \quad -0.15 \quad -0.2)$
ζ	Modal Damping Ratio of Solar Panels	$\text{diag}(0.009 \quad 0.0138 \quad 0.02083 \quad 0.04)$
$\Omega(\text{Hz})$	Fundamental Frequencies of Solar Panels	$\text{diag}(0.15853 \quad 0.44764 \quad 0.86703 \quad 0.96188)$
B_t	Translational Coupling Matrix of Solar Panels	$\begin{pmatrix} 0.0706 & 7.2756 & -1.0032 & -0.0134 \\ 0.2283 & 0.1923 & -0.0682 & -1.6051 \\ 6.9815 & -0.0017 & -0.0936 & -3.8853 \end{pmatrix}$
B_r	Rotational Coupling Matrix of Solar Panels	$\begin{pmatrix} -44.7546 & 0.2369 & 0.2179 & 9.6937 \\ 0.2404 & -12.1033 & -5.9076 & -0.013 \\ 0.4144 & 45.8615 & -5.6713 & 0.0151 \end{pmatrix}$
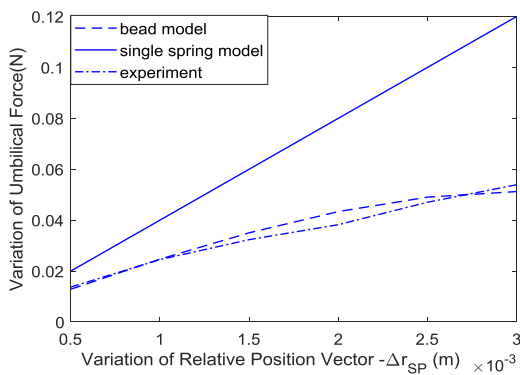
FIGURE 7. Variation of umbilical force versus variation of relative position vector $-\Delta\rho_{\text{SP}}$.

system with umbilical connection (Case 1) are conducted. Moreover, to study the impact of the umbilical and translational coupling between solar panels and SM on pointing performance of DFP system, simulation studies include two other cases, Case 2 (DFP system without umbilical connection) and Case 3 (DFP system with umbilical connection

but do not take translational coupling between solar panels and SM into account). It should be noted that bead model is used for modeling the umbilical connection between support module and payload module in both Case 1 and Case 3 while it is not applied in Case 2 since no umbilical connection is considered in Case 2. Motion equations including kinematic equations and dynamic equations for both Case 2 and Case 3 are given before simulation results demonstration. Simulation conditions and control system parameters are listed in Table 1 and Table 2, respectively. The parameters associated with support module and coupling matrices of solar panels can be referred to Ref [25]. It should be noted that, in order to facilitate the analysis, only the first four modal coordinates of the solar panels are considered.

A. CASE 1
Motion equations consisting of kinematic equations and dynamic equations for PM, SM and beads in Case 1 are given in (18), (19), (20), (21), (23) and (24). Simulation results associated with Case 1 are shown from Fig. 8 to Fig. 11. Fig. 8 depicts time history of relative position error of the DFP system, whereas Fig. 9 presents time history of umbilical

TABLE 2. Control system parameters.

Parameter	Parameter Name	Value
	PM Attitude Control Loop	
K_{PP}	Proportional Gain of PM Attitude Control Loop	$3\times10^4\times\mathrm{diag}\begin{pmatrix}1&1&1\end{pmatrix}$
K_{PD}	Derivative Gain of PM Attitude Control Loop	$3\times10^4\times\mathrm{diag}\begin{pmatrix}1&1&1\end{pmatrix}$
q_{Pv0}	Desired Vector Part of PM Quaternion	$\begin{pmatrix}0&0&0\end{pmatrix}$
$\omega_{P0}\,(°/s)$	Desired PM Angular Velocity	$\begin{pmatrix}0&0&0\end{pmatrix}$
	Relative Position Control Loop	
K_{RTP}	Proportional Gain of Relative Position Control Loop	$10^4\times\mathrm{diag}\begin{pmatrix}1&1&1\end{pmatrix}$
K_{RTD}	Derivative Gain of Relative Position Control Loop	$10^3\times\mathrm{diag}\begin{pmatrix}1&1&1\end{pmatrix}$
$\rho_{SP0}\,(m)$	Desired Relative Position Vector	$\begin{pmatrix}0.799&-0.248&-0.301\end{pmatrix}$
$\dot{\rho}_{SP0}\,(m/s)$	Desired Relative Velocity Vector	$\begin{pmatrix}0&0&0\end{pmatrix}$
	Relative Attitude Control Loop	
K_{RAP}	Proportional Gain of Relative Attitude Control Loop	$5\times10^2\times\mathrm{diag}\begin{pmatrix}1&1&1\end{pmatrix}$
K_{RAD}	Derivative Gain of Relative Attitude Control Loop	$5\times10^2\times\mathrm{diag}\begin{pmatrix}1&1&1\end{pmatrix}$
q_{Rv0}	Desired Vector Part of Relative Quaternion	$\begin{pmatrix}0&0&0\end{pmatrix}$
$\omega_{R0}\,(°/s)$	Desired Relative Angular Velocity	$\begin{pmatrix}0&0&0\end{pmatrix}$
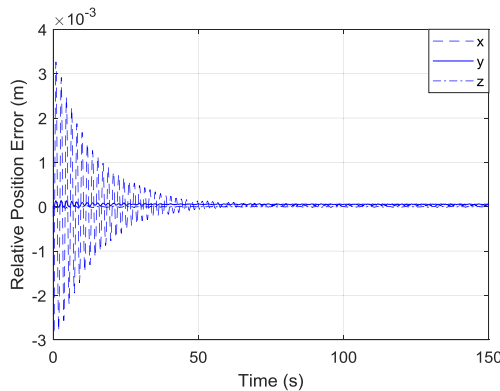
FIGURE 8. Time history of relative position error of DFP system (case 1).

TABLE 3. Pointing performance of DFP system (Case 1).

Pointing Performance	Support Module	Payload Module
Pointing Accuracy (°)	5×10^{-2}	4×10^{-4}
Pointing Stability (°/s)	4×10^{-3}	2.5×10^{-4}

moments acting on SM and PM. Moreover, Fig. 10 and Fig. 11 illustrate time history of attitude and angular velocity of the DFP system, respectively.

As can be seen in Fig. 8, the norm of three components of relative position error are kept within 4 mm which indicates that the control system designed in this paper can well satisfies the noncontact actuator's working range requirement ($\leq$ 5 mm) [18]. In Fig. 9, it can be observed that the umbilical moments acting on SM and PM over the time history are kept within 1 N · m and 0.6 N · m, respectively. According to the results in Fig. 10 and Fig. 11, pointing performance of the DFP system is summarized in Table 3.

As can be seen, both pointing accuracy and pointing stability of PM are of an order of -4. And their counterparts of SM are of an order of -2 and -3, respectively. It is obvious that pointing accuracy of PM appears to be 2 orders better than its counterpart of SM whereas pointing stability of PM achieves

increase of 1 order. The fact that pointing performance of PM rivals its counterpart of SM verifies the effectiveness of DFP configuration in isolating vibrations transmitted from SM to PM.

Although each PD controller has only two parameters, controller tunings in this paper are not easy since three PD controllers are needed and their control loops are coupled which can be clearly seen in Fig. 3. To address the tuning challenge, some simple rules and insight for each PD controller are presented in this paper. In addition, to give a clear illustration of influences of different control parameters selection on the control performance, simulation applying different control parameters are conducted and compared.

For payload attitude control loop, the control gains (K_{PP} and K_{PD}) are determined by a trade-off between high pointing performance of payload module and small control output (T_{Pc}). Simulation applying different control gains are conducted and results comparison are summarized in Table 4.

The results comparison in Table 4 indicates that higher values of control gains (K_{PP} and K_{PD}) contribute to achieving better pointing performance while higher values of control gains demand higher control output.

For relative translation control loop, the control gains (K_{RTP} and K_{RTD}) are determined by a trade-off between
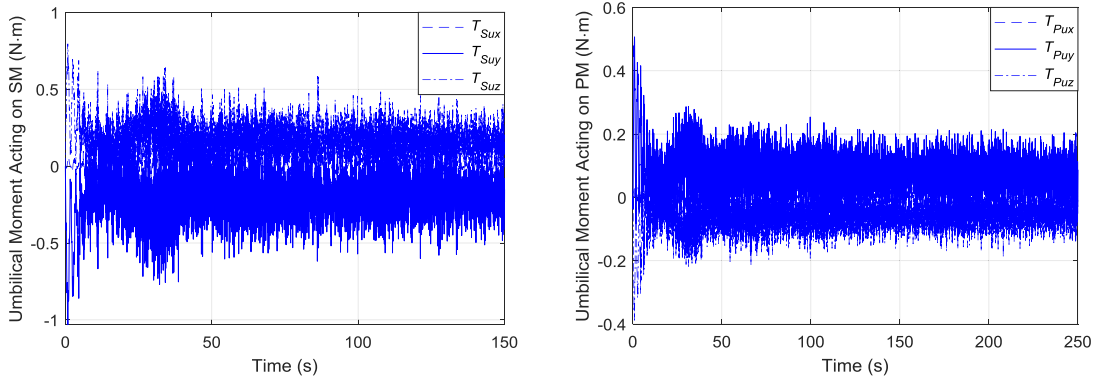
FIGURE 9. Time history of umbilical moments acting on SM and PM (case 1): a) umbilical moment acting on SM, b) umbilical moment acting on PM.
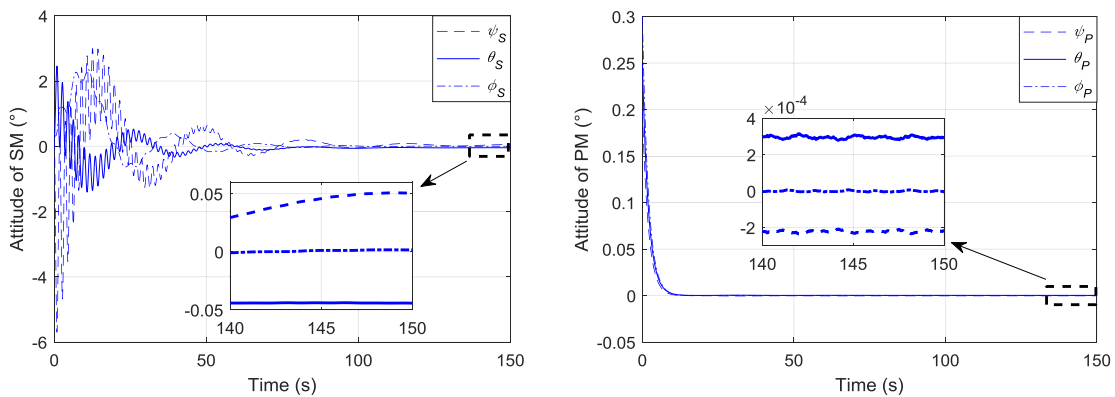

FIGURE 10. Time history of attitude of DFP system (case 1): a) attitude of SM, b) attitude of PM.
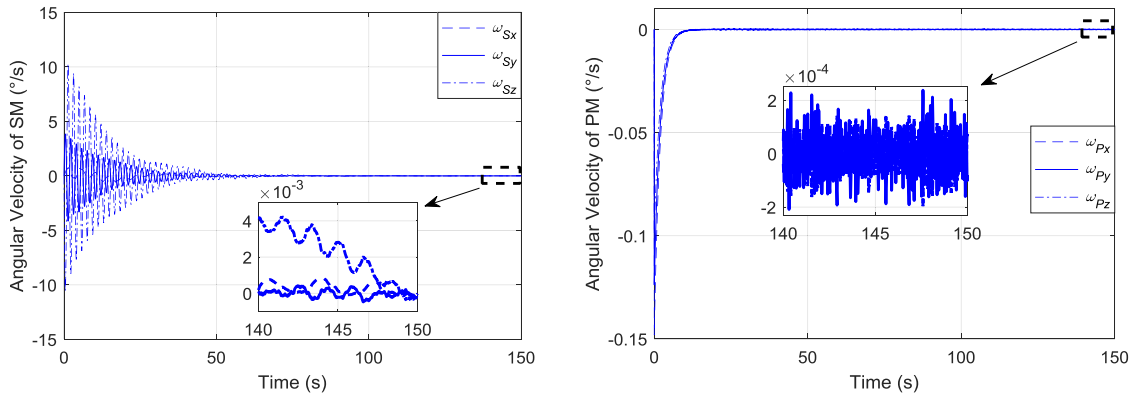

FIGURE 11. Time history of angular velocity of DFP system (case 1): a) angular velocity of SM, b) angular velocity of PM.

requirement on relative position error and small control output (F_{Pc}). Simulation applying different control gains are conducted and results comparison are summarized in Table 5.

The results comparison in Table 5 indicates that higher values of control gains (K_{RTP} and K_{RTD}) contribute to lower relative position error while higher values of control gains demand higher control output.

For relative attitude control loop, the control gains (K_{RAP} and K_{RAD}) are determined by a trade-off between

requirement on relative position error and small control output (T_{Sc}). Simulation applying different control gains are conducted and results comparison are summarized in Table 6.

The results comparison in Table 6 indicates that higher values of control gains (K_{RAP} and K_{RAD}) contribute to lower relative position error while higher values of control gains demand higher control output.

To the best of authors' knowledge, experimental test of DFP system is limited on the stage of ground test [12], [13].

TABLE 4. Simulation results comparison between different control gains for payload attitude control loop.

Performance	$K_{PP}=3\times10^4\text{diag}(1\ \ 1\ \ 1)$ $K_{PD}=3\times10^4\text{diag}(1\ \ 1\ \ 1)$	$K_{PP}=3.5\times10^4\text{diag}(1\ \ 1\ \ 1)$ $K_{PD}=3.5\times10^4\text{diag}(1\ \ 1\ \ 1)$
Pointing Accuracy (°)	4×10^{-4}	2.791×10^{-4}
Pointing Stability (°/s)	2.5×10^{-4}	1.85×10^{-4}
Maximum Control Output (N·m)	4.251	18.28

TABLE 5. Simulation results comparison between different control gains for relative translation control loop.

Performance	$K_{RTP}=10^4\text{diag}(1\ \ 1\ \ 1)$ $K_{RTD}=10^3\text{diag}(1\ \ 1\ \ 1)$	$K_{RTP}=2\times10^4\text{diag}(1\ \ 1\ \ 1)$ $K_{RTD}=2\times10^3\text{diag}(1\ \ 1\ \ 1)$
Relative Position Error (m)	3.27×10^{-3}	2.1×10^{-3}
Maximum Control Output (N)	34.3	35.14

TABLE 6. Simulation results comparison between different control gains for relative attitude control loop.

Performance	$K_{RAP}=5\times10^2\text{diag}(1\ \ 1\ \ 1)$ $K_{RAD}=5\times10^2\text{diag}(1\ \ 1\ \ 1)$	$K_{RAP}=8\times10^2\text{diag}(1\ \ 1\ \ 1)$ $K_{RAD}=8\times10^2\text{diag}(1\ \ 1\ \ 1)$
Relative Position Error (m)	3.27×10^{-3}	3.23×10^{-3}
Maximum Control Output (N·m)	107.5	167.1

TABLE 7. Pointing performance comparison of payload module between simulation and ground test.

Pointing Performance	Simulation	Ground Test
Pointing Accuracy (°)	4×10^{-4}	8×10^{-3}
Pointing Stability (°/s)	2.5×10^{-4}	3.5×10^{-3}

No on-orbit test of DFP system is performed, mainly due to premature of DFP technology. With the help from Shanghai Satellite Engineering Institute, ground test data of DFP system is obtained. Then, pointing performance of payload module obtained from simulation (Case 1) and ground test data are listed in Table 7 for comparison.

It can be seen from Table 7 that pointing performance obtained from simulation appears to be 1 order better than its counterpart obtained from ground test. As is mentioned in Section III-B, external disturbances acting on payload module in the simulation comprise of atmospheric drag and

TABLE 8. Simulation results comparison between case 1 and case 2.

Performance	Case 1		Case 2	
	Support Module	Payload Module	Support Module	Payload Module
Pointing Accuracy (°)	5×10^{-2}	4×10^{-4}	1.7×10^{-2}	4×10^{-9}
Pointing Stability (°/s)	4×10^{-3}	2.5×10^{-4}	4×10^{-3}	2×10^{-11}
Relative Position Error (m)	$\leq3.27\times10^{-3}$		$\leq3\times10^{-3}$	

gravity gradient moment. Immune to atmospheric drag and gravity gradient moment, however, payload module in ground testing system is mainly affected by its surrounding environment, including vibrations and disturbance resulted from thermal environment and magnetic environment. Therefore, environment in the ground testing system that varies its counterpart in the simulation, results in the performance difference between simulation and ground testing.

B. CASE 2

Without umbilical connection in Case 2, kinematic and dynamic equations of PM are given as:

$$\dot{r}_P = v_P$$
$$\dot{q}_P = \frac{1}{2}q_P \otimes \varpi_P \qquad (25)$$
$$M_P\dot{v}_P = M_P a_P = F_{Pg} + F_{Pd} + F_{Pc}$$
$$I_P\dot{\omega}_P = -\omega_P \times (I_P\omega_P) + T_{Pd} + T_{Pc} \qquad (26)$$

Similarly, kinematic and dynamic equations of SM are presented as:

$$\dot{r}_S = v_S$$
$$\dot{q}_S = \frac{1}{2}q_S \otimes \varpi_S \qquad (27)$$
$$M_S\dot{v}_S + B_t\ddot{\eta} = F_{Sg} + F_{Sd}$$
$$I_S\dot{\omega}_S + B_r\ddot{\eta} = -\omega_S \times (I_S\omega_S) + T_{Sd} + T_{Sc}$$
$$\ddot{\eta}+2\zeta\Omega\dot{\eta}+\Omega^2\eta+B_t^T a_S+B_r^T\dot{\omega}_S = 0 \qquad (28)$$

Time history of relative position error, attitude and angular velocity of DFP system in Case 2 are not depicted due to limited space. However, Table 8 summarizes simulation results associated with Case 2 as well as their counterparts in Case 1 for comparison.

In contrast to Case 1, pointing accuracy of PM in Case 1 degrades by 5 orders while pointing stability decreases by 7 orders. Concerning performance of SM, both of Case 1 and Case 2 are of same orders, i.e. an order of -2 for pointing accuracy and an order of -4 for pointing stability. In addition, both cases show roughly the same performance with respect to upper limit of relative position error, i.e. 3.27 mm in Case 1 and 3 mm in Case 2.

It can be concluded that umbilical connection dramatically lower pointing performance of PM whereas it exerts

TABLE 9. Simulation results comparison between case 1 and case 3.

Performance	Case 1		Case 3	
	Support Module	Payload Module	Support Module	Payload Module
Pointing Accuracy (°)	5×10^{-2}	4×10^{-4}	2×10^{-3}	5×10^{-6}
Pointing Stability (°/s)	4×10^{-3}	2.5×10^{-4}	2×10^{-4}	2.25×10^{-6}
Relative Position Error (m)	$\leq 3.27 \times 10^{-3}$		$\leq 7 \times 10^{-5}$	
Umbilical Moment on SM (N·m)	≤ 1		$\leq 5.1 \times 10^{-1}$	
Umbilical Moment on PM (N·m)	$\leq 10^{-2}$		$\leq 4 \times 10^{-3}$	

insignificant impact on pointing performance of SM. Working as necessary unit for data, energy and liquid transfer in DFP system, however, the umbilical connection has a serious side-effect of introducing disturbance and vibrations from SM to PM. Moreover, the roughly same performance of upper limit of relative position error indicates that umbilical connection has little influence on relative position motion between SM and PM.

C. CASE 3

The only difference between Case 3 and Case 1 lies in that Case 3 does not consider translational coupling between solar panels and SM. Therefore, motion equations including kinematic equations and dynamic equations in Case 3 can simply refer to their counterpart in Case 1 except the dynamic equations for SM. Dynamic equations for SM in Case 3 can be obtained by rewriting (21) as:

$$M_S \dot{v}_S = F_{Sg} + F_{Sd} + F_{Su}$$
$$I_S \dot{\omega}_S + B_r \ddot{\eta} = -\omega_S \times (I_S \omega_S) + T_{Sd} + T_{Su} + T_{Sc}$$
$$\ddot{\eta} + 2\zeta \Omega \dot{\eta} + \Omega^2 \eta + B_r^T \dot{\omega}_S = 0 \qquad (29)$$

Simulation results associated with Case 3 and Case 1 are listed in Table 9 for comparison.

It is clear that all the results in Case 3 appear to be 1 to 2 orders smaller than their counterparts in Case 1. To be specific, pointing performance (including pointing accuracy and pointing stability) of SM in Case 1 are 1 order lower than that in Case 3, whereas pointing performance of PM in Case 1 show 2 orders decrease than that in Case 3. Besides, relative position error in Case 1 is two orders higher than that in Case 3. Similarly, both umbilical moments acting on SM and PM in Case 1 are 1 order larger than their counterparts in Case 3. Therefore, translational coupling between solar panels and SM degrades pointing performance of DFP system. It should be noted that translational coupling between solar panels and SM acts to increase the relative position error which results in a higher level of umbilical moments. As a result, higher level of umbilical moments leads to significant pointing performance degradation.

VI. CONCLUSION

This paper aims at gaining insight into the impact of umbilical and translational coupling of solar panels on pointing performance of Disturbance-Free-Payload (DFP) system. Bead model is utilized to represent dynamics of umbilical and is incorporated into the multibody rigid-flexible dynamics of the DFP system. The dynamics of solar panels are derived by using hybrid coordinate method and the translational coupling between solar panels and support module is specifically considered.

Simulation studies indicate that umbilical connection degrades pointing performance of DFP system in two aspects. Firstly, it directly applies umbilical forces and moments on support module and payload module. Secondly, umbilical connection works as a channel that introduces disturbance and vibrations (such as elastic vibrations of the solar panels in this paper) transmitted from support module to payload. An accurate umbilical model (e.g. bead model in this paper) not only plays a critical part in obtaining correct pointing performance of DFP system, but contributes to validating the effectiveness of DFP high-precise control methods.

Considerable attention in future work should be paid to pointing performance improvement of DFP system under the impact of umbilical connection and solar panels.

REFERENCES

[1] L. Jones-Wilson, S. Susca, C. Diaz, H. Chang, E. Duffy, R. Effinger, D. Lewis, K. Liewer, K. Lo, H. Ochoa, and J. Perez, "A sub-arcsecond pointing stability fine stage for a high altitude balloon platform," in *Proc. IEEE Aerosp. Conf.*, Mar. 2017, p. 1. doi: 10.1109/AERO.2017.7943590.

[2] B. Xiao, S. Yin, and O. Kaynak, "Attitude stabilization control of flexible satellites with high accuracy: An estimator-based approach," *IEEE/ASME Trans. Mechatronics*, vol. 22, no. 1, pp. 349–355, Feb. 2017. doi: 10.1109/TMECH.2016.2614839.

[3] N. Yoshida, O. Takahara, and K. Kodeki, "Spacecraft with very high pointing stability: Experiences and lessons learned," *IFAC Proc. Vol.*, vol. 46, no. 19, pp. 547–556, Sep. 2013. doi: 10.3182/20130902-5-DE-2040.00144.

[4] Y. Zhang, M. Li, and J. Zhang, "Vibration control for rapid attitude stabilization of spacecraft," *IEEE Trans. Aerosp. Electron. Syst.*, vol. 53, no. 3, pp. 1308–1320, Jun. 2017. doi: 10.1109/TAES.2017.2670798.

[5] F. Malbet *et al.*, "High precision astrometry mission for the detection and characterization of nearby habitable planetary systems with the Nearby Earth Astrometric Telescope (NEAT)," *Experim. Astron.*, vol. 34, no. 2, pp. 385–413, 2012. doi: 10.1007/s10686-011-9246-1.

[6] L. J. Romualdez, "Precise pointing and stabilization performance for the balloon-borne imaging testbed: 2015 test flight," *Proc. Inst. Mech. Eng. G, J. Aerosp. Eng.*, vol. 231, no. 4, pp. 713–723, Mar. 2017. doi: 10.1177/0954410016641451.

[7] Z. Wu, X. Jing, B. Sun, and F. Li, "A 6DOF passive vibration isolator using X-shape supporting structures," *J. Sound Vib.*, vol. 380, pp. 90–110, Oct. 2016. doi: 10.1016/j.jsv.2016.06.004.

[8] L. Wang, J. Li, Y. Yang, J. Wang, and J. Yuan, "Active control of low-frequency vibrations in ultra-precision machining with blended infinite and zero stiffness," *Int. J. Mach. Tools Manuf.*, vol. 139, pp. 64–74, Apr. 2019. doi: 10.1016/j.ijmachtools.2018.11.004.

[9] L. Li, J. Zhang, and R. Luo, "Modeling and blind source separation analysis of a vibration isolation system for spacecraft," in *Proc. IEEE Int. Conf. Adv. Intell. Mechatron.*, Jul. 2017, pp. 1711–1719. doi: 10.1109/AIM.2017.8014265.

[10] F. Wang, Z. Weng, and L. He, "Active and passive hybrid vibration isolation," in *Comprehensive Investigation on Active-Passive Hybrid Isolation and Tunable Dynamic Vibration Absorption*. Singapore: Springer, 2019, pp. 19–40. doi: 10.1007/978-981-13-3056-8.

[11] N. Pedreiro, "Spacecraft architecture for disturbance-free payload," *J. Guid., Control, Dyn.*, vol. 26, no. 5, pp. 794–803, Sep. 2003. doi: 10.2514/2.5114.

[12] M. Gonzales, N. Pedreiro, K. Brookes, D. Roth, and B. Foster, "Unprecedented vibration isolation demonstration using the disturbance-free payload concept," in *Proc. AIAA Guid., Navigat., Control Conf. Exhibit*, Aug. 2004, p. 5247. doi: 10.2514/6.2004-5247.

[13] M. Regehr, "Analysis of a near-free-floating vibration isolation platform," in *Interplanetary Network Progress Report*, Washington, DC, USA: NASA, vol. 2015.

[14] C. Wu, X. Kong, Y. Liu, and Z. Chen, "Coupling characteristics analysis for the disturbance free payload spacecraft," *Acta Astronautica.*, vol. 138, pp. 407–416, Sep. 2017. doi: 10.1016/j.actaastro.2017.06.020.

[15] Y. Pang, J. Li, and L. Liu, "Dynamics modeling of the separated satellite with flexible cable," *J. Astronaut.*, vol. 38, pp. 1–5, Apr. 2017. doi: 10.3873/j.issn.1000-1328.2017.01.001.

[16] J. Zhou, L. Liu, Z. Wang, J. Li, H. Liao, and Y. Deng, "On pointing accuracy and pointing stability of disturbance-free payload using umbilical connection," in *Proc. 37th Chin. Control Conf. (CCC)*, Jul. 2018, pp. 1591–1598. doi: 10.23919/ChiCC.2018.8482705.

[17] J. Wang, D. Li, and J. Jiang, "Optimal variable amplitudes input shaping control for slew maneuver of flexible spacecraft," *J. Guid., Control, Dyn.*, vol. 40, no. 12, pp. 3255–3268, Dec. 2017. doi: 10.2514/1.G002838.

[18] T. Trankle, N. Pedreiro, and G. Andersen, "Disturbance free payload flight system analysis and simulation methods," in *Proc. AIAA Guid., Navigat., Control Conf. Exhibit*, Aug. 2005, p. 5875. doi: 10.2514/6.2005-5875.

[19] J. T. Carter and M. Greene, "Simulation of single tether systems," *Simul. Trans. Soc. Model.*, vol. 58, no. 1, pp. 42–48, 1992. doi: 10.1177/003754979205800107.

[20] Y. Xu, H. Liao, L. Liu, and Y. Wang, "Modeling and robust H-infinite control of a novel non-contact ultra-quiet Stewart spacecraft," *Acta Astronautica*, vol. 107, pp. 274–286, Mar. 2015. doi: 10.1016/j.actaastro.2014.11.033.

[21] N. Sun, T. Yang, Y. Fang, Y. Wu, and H. Chen, "Transportation control of double-pendulum cranes with a nonlinear quasi-PID scheme: Design and experiments," *IEEE Trans. Syst., Man, Cybern. Syst.*, vol. 49, no. 7, pp. 1408–1418, Jul. 2019. doi: 10.1109/TSMC.2018.2871627.

[22] T. Yang, N. Sun, H. Chen, and Y. Fang, "Neural network-based adaptive antiswing control of an underactuated ship-mounted crane with roll motions and input dead zones," *IEEE Trans. Neural Netw. Learn. Syst.*, to be published. doi: 10.1109/TNNLS.2019.2910580.

[23] J. Zhou, L. Liu, and Z. Wang, "Modeling and analysis of ultra-low frequency dynamics of drag-free satellites," *Microgravity Sci. Technol.*, vol. 31, no. 2, pp. 151–160, 2019. doi: 10.1007/s12217-019-9672-7.

[24] A. Chaves-Jiménez, J. Guo, and E. Gill, "Impact of atmospheric coupling between orbit and attitude in relative dynamics observability," *J. Guid., Control, Dyn.*, vol. 40, no. 12, pp. 3274–3281, Dec. 2017. doi: 10.2514/1.G002618.

[25] W. Lv, M. Xiang, W. Ye, Y. Wen, and H. Zhu, "Research on calculation of on-orbit unconstraint modal of flexible satellite," *J. Astronaut.*, April., vol. 35, no. 4, pp. 404–408, 2014. doi: 10.3873/j.issn.1000-1328.2014.04.005.

ZHIGANG WANG received the B.Eng., M.Eng., and Ph.D. degrees from the School of Astronautics, Northwestern Polytechnical University, Xi'an, China, in 1991, 1994, and 1998, respectively, where he has been a Professor, since 2004. His research interests include dynamics modeling and control of spacecraft and aircraft, aerodynamics, and active vibration isolation.
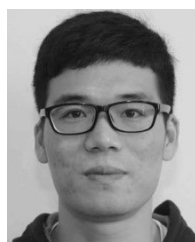
WEI LI received the B.Eng. and Ph.D. degrees from the School of Astronautics, Northwestern Polytechnical University, Xi'an, China, in 2007 and 2014, respectively, where he has been an Assistant Professor, since 2014. His research interests include dynamics modeling and control of spacecraft and aircraft, aerodynamics, and trajectory optimization of aircraft.

LEI LIU received the B.Eng. and Ph.D. degrees from the Harbin Institute of Technology, China, in 2005 and 2011, respectively, and the Ph.D. degree with the National University of Singapore, in 2012. He is currently a Professor with the School of Astronautics, Northwestern Polytechnical University, Xi'an, China. His research interests include modeling, identification and control of precision motion systems, spacecraft dynamic and control, active vibration isolation, and electro-optical system control.

YIFAN DENG received the B.Eng., M.Eng., and Ph.D. degrees from the School of Astronautics, Northwestern Polytechnical University, Xi'an, China, in 2009, 2012, and 2016, respectively. Since 2018, he has been a Postdoctoral Researcher with the School of Electronic and Information Engineering, Xi'an Jiaotong University, Xi'an, China. His research interests include dynamics modeling and control of spacecraft and aircraft, and optimal estimation.

JIAXING ZHOU received the B.Eng. and M.Eng. degrees from the School of Astronautics, Northwestern Polytechnical University, Xi'an, China, in 2012 and 2015, respectively, where he is currently pursuing the Ph.D. degree. His research interests include dynamics modeling and control of spacecraft and aircraft, and active vibration isolation.

QIANG ZHAO received the B.Eng. degree from Shandong University, Jinan, China, in 2011, and the M.Eng. degree from Beihang University, Beijing, China, in 2014. Since 2014, he has been an Engineer with the Shanghai Institute of Satellite Engineering, Shanghai, China. His research interests include attitude control of spacecraft and motor control.

• • •